Highlighting the processing versatility of a silicon phthalocyanine derivative for organic thin-film transistors

Rosemary R. Cranston,[a] Benjamin King,[a] Chloé Dindault,[a] Trevor M. Grant,[a] Nicole A. Rice,[a] Claire Tonnelé,[b] Luca Muccioli,[cd] Frédéric Castet,[c] Sufal Swaraj,[e] and Benoît H. Lessard*[af]

[a] *Department of Chemical and Biological Engineering, University of Ottawa, 161 Louis Pasteur, Ottawa, ON, K1N 6N5, Canada. E-mail: benoit.lessard@uottawa.ca*
[b] *Donostia International Physics Center, 4 Paseo Manuel de Lardizabal, 20018 Donostia, Euskadi, Spain*
[c] *Univ. Bordeaux, CNRS, Bordeaux INP, ISM, UMR 5255, F-33400 Talence, France*
[d] *University of Bologna, Department of Industrial Chemistry, 4 Viale Risorgimento, 40136 Bologna, Italy*
[e] *SOLEIL Synchrotron, L'Orme des Merisiers, Saint-Aubin, P.O. Box 48, CEDEX, FR-91192 Gif-Sur-Yvette, France*
[f] *School of Electrical Engineering and Computer Science, University of Ottawa, 800 King Edward, Ottawa, ON, K1N 6N5, Canada*

† Electronic supplementary information (ESI) available. CCDC 2091746 and 2067659. For ESI and crystallographic data in CIF or other electronic format see DOI: 10.1039/d1tc05238a

Silicon phthalocyanine (SiPc) derivatives have recently emerged as promising materials for n-type organic thin-film transistors (OTFTs) with the ability to be fabricated either by solid state or solution processes through axial functionalization. Among those, bis(tri-n-propylsilyl oxide) SiPc ((3PS)$_2$-SiPc) is unique as it can be processed by sublimation, while being soluble enough for solution processing. In this work, the charge transport properties of (3PS)$_2$-SiPc and its polymorphic forms were studied through Kinetic Monte Carlo (KMC) simulations and density functional theory (DFT) calculations along with the characterization of (3PS)$_2$-SiPc in n-type OTFTs fabricated by physical vapour deposition (PVD) and spin coating. Post-deposition thin-film characterization by X-ray diffraction (XRD), atomic force microscopy (AFM), and scanning transmission X-ray microscopy (STXM) was used to assess film morphology and microstructure in relation to the electrical performance of OTFTs. The differences in film formation by PVD and solution fabrication had little effect on OTFT performance with comparable field-effect mobility and threshold voltage ranging between 0.01–0.04 cm2 V^{-1} s^{-1} and 18–36 V respectively. Consistent charge transport properties of (3PS)$_2$-SiPc OTFTs achieved at different fabrication conditions highlights the processing versatility of this material.

Introduction

Since the 1980s organic thin-film transistors (OTFTs) using conjugated polymer and small molecule materials have been envisioned as an improved technology to traditional inorganic silicon and germanium transistors.[1,2] The low switching speed and charge carrier mobility of many organic semiconducting materials contribute to the fact that OTFTs are meant to supplement inorganic technologies, and advance novel applications requiring large areas, high flexibility, less energy intensive processing conditions, and low cost. Most notably, OTFTs serve as the main component of inexpensive flexible electronic circuits facilitating the design of state-of-the-art bio- logical sensors,[3–5] wearable electronics,[6–8] and flexible displays.[9–11] An applied positive or negative voltage can yield either an accumulation of holes or electrons in the intrinsically semiconducting materials used in OTFTs, resulting in n- or p-type transistor behaviour. For many organic small molecules p-type transistor operation is dominant, however through the synthesis of materials with high electron affinities significant advances have been made in the development of n-type OTFTs. Unfortunately, many n-type behaving materials demonstrate lower mobilities, worse environ- mental/chemical stability, and lower solubility compared to materials for p-type OTFTs, making them impractical for many applications.[12,13]

Metal or metalloid phthalocyanines (MPcs) are a vast group of semiconducting organic small molecules comprised of a conjugated aromatic structure with a central chelated metal ion. For over 90 years MPcs have been used extensively as dyes, pigments, and more recently as commercial photoreceptors owing to their brilliant colour, ease of synthesis, favourable opto-electric properties, and high thermal, mechanical, and environmental stability.[14] Compared to divalent MPcs, silicon phthalocyanine (SiPc) derivatives offer two additional axial positions for

added molecular tunability. Additionally, SiPcs possess n-type semiconducting behaviour rather than the more common p-type behaviour demonstrated by most MPc based OTFTs. The high thermal stability of phenoxy substituted SiPcs have enabled the fabrication of n-type OTFTs by physical vapour deposition (PVD) with a maximum mobility of 0.54 $cm^2\ V^{-1}\ s^{-1}$ achieved by bis(pentafluorophenoxy) SiPc (F_{10}-SiPc).[15–18] Phenoxy substituted SiPcs have also demon- strated promising results in mixed PVD and solution fabricated organic photovoltaic devices (OPVs) exhibiting an open-circuit voltage (V_{oc}) of 0.88 V.[19] The highly soluble alkyl substituted SiPc derivatives have been used for solution fabricated n-type OTFTs[20,21] and OPVs,[22,23] with bis(tri-*n*-butylsilyl oxide) SiPc ($(3BS)_2$-SiPc) demonstrating the highest performance in both types of devices. Bis(tri-*n*-propylsilyl oxide) SiPc ($(3PS)_2$-SiPc) is a unique derivative as its synthetic simplicity, scalable syn- thesis, n-type behaviour, high solubility, and high thermal stability makes it an exceedingly versatile material (Fig. 1).[24] Unlike previously reported SiPcs,[25] $(3PS)_2$-SiPc possesses unique processing duality facilitating fabrication by both PVD and solution processing, owing to its ability to sublime without decomposing and its high solubility in chlorinated solvents (15 mg mL^{-1}).[24] These features of $(3PS)_2$-SiPc allow for easy purification and a multitude of choice for device fabrication processing methods and conditions.

Herein, the fabrication and characterization of PVD and solution fabricated bottom-gate top-contact (BGTC) $(3PS)_2$- SiPc OTFTs are reported. The performance of PVD and solution fabricated devices was compared through post-deposition characterization by thin-film X-ray diffraction (XRD) and atomic force microscopy (AFM). Additionally, scanning transmission X-ray microscopy (STXM) was used to elucidate the distribution of $(3PS)_2$-SiPc molecules in films fabricated from solution. Kinetic Monte Carlo (KMC) simulations and density functional theory (DFT) calculations were performed to evaluate the crystal structure and access the charge transport dimensionality of each poly- morphic form of $(3PS)_2$-SiPc and related to OTFT characterization. This work aims to highlight the fabrication versatility and excep- tional performance of $(3PS)_2$-SiPc in OTFTs with hopes to further the advancement of high performing n-type MPc based organic electronic devices.

Results and discussion

Quantum chemical calculations

Transport levels, optical properties and charge transport para- meters of the $(3PS)_2$-SiPc molecule were first studied with DFT and time-dependent (TD) DFT calculations. The highest occupied molecular orbital (HOMO), lowest unoccupied molecular orbital (LUMO), and LUMO+1 energies, equaling —5.11 eV,

2.92 eV, and 2.91 eV respectively, are close to those of similar alkylsiloxy-substituted SiPcs[21] and rather appropriate for ambipolar transport. Vertical transition energies (DE) and oscillator strengths (f) from the ground state S_0 towards the nearly degenerate singlet states S_1 and S_2 of $(3PS)_2$-SiPc were calculated to be DE_{01} (f_{01}) = 2.057 eV (0.33) and DE_{02} (f_{02}) = 2.061 eV (0.34). The electron affinity (EA) of $(3PS)_2$-SiPc, equal to 1.99 eV, is again very similar to EA values calculated for previously reported MPcs.[21] However, the internal charge transfer reorganization energy (l = 210 meV), which characterizes the amplitude of geometric relaxation effects occurring upon electron transfer, is slightly lower than those previously reported for other alkylsiloxy-substituted SiPcs (213–266 meV).[21] Compared to these materials, electron delocalization in the frame of an activated hopping-like transport is thus expected to be slightly more favoured in $(3PS)_2$-SiPc (eqn (1)). The largest electronic couplings (transfer integrals) calculated between molecular neighbours in polymorphs 1 and 2 are shown in Fig. 2, while the complete set of non-negligible J_e values are reported in Table S1 and S2 (ESI†). The largest coupling in polymorph 1 amounts to 7.6 meV and occurs between molecules stacked parallel to the (0; ±0.5; ±0.5) directions. In polymorph 2, the highest J_e value is found along the (±1; 0; 0) direction, *i.e.* parallel to the *a* crystal axis, with a larger magnitude of 11.4 meV. As reported in Table S1 and S2 (ESI†), rather large electronic couplings (10.1 eV) also exist in polymorph 2 along the (±0.5; ±0.5; ±0.5) directions.

On the contrary, these secondary transfer integrals are much lower in polymorph 1 (1.6 meV, along the *a* axis), which makes polymorph 2 more prone to display efficient and multidimensional charge transport. This is confirmed by the calculated electron mobilities reported in Table S3 (ESI†) and Fig. 3: besides having mobilities approximately three times lower, polymorph 1 is almost not conducing along the *a* axis, as a consequence of the above mentioned small transfer integrals. These results suggest that charge transport through $(3PS)_2$-SiPc should be highly dependent on the amount and nature of the polymorphs which are present in the device.

Organic thin-film transistors

BGTC OTFTs were fabricated on silicon substrates with a dielectric layer comprised of thermally grown silicon oxide. $(3PS)_2$-SiPc thin-films were deposited by either PVD or spin coating and annealed to create the semiconducting active layer. All OTFT electrical characterization was performed in a nitrogen environment at room temperature to obtain the saturation regime electron field-effect mobility (m_e), threshold voltage (V_T) and on/off current ratio ($I_{on/off}$) of each transistor with results displayed in Table 1. Characteristic output curves, as well as forward and reverse transfer curves of PVD and solution fabricated OTFTs are displayed in Fig. S4 and S5 (ESI†) respectively. OTFTs made by both fabrication methods resulted in remarkably similar electrical performance with average mobilities in the range of 1.0–3.9 × 10^{-2} cm^2 V^{-1} s^{-1} for PVD devices and 2.3–4.1 × 10^{-2} cm^2 V^{-1} s^{-1} for solution, with threshold voltages between 18 V and 32 V for both methods. In comparison to other BGTC bis(tri-alkylsilyl oxide) SiPc OTFTs which exhibit average mobilities ranging from 10^{-4}– 10^{-2} cm^2 V^{-1} s^{-1} and threshold voltages between 20–40 V,[21] $(3PS)_2$-SiPc OTFTs displayed comparable or superior electrical performance. All OTFTs exhibited consistently high $I_{on/off}$, between 10^4–10^5, suitable for device operation and comparable to that of other SiPc OTFTs fabricated by both solution and evaporative processing.[17,21] To date, the highest performing solution fabricated SiPc OTFT was reported with $(3BS)_2$-SiPc exhibiting a $m_{e,max}$ of 4.3 × 10^{-2} cm^2 V^{-1} s^{-1}, $m_{e,avg}$ of 2.8 × 10^{-2} cm^2 V^{-1} s^{-1} and V_T of 17.6 V.[21] However, the $(3PS)_2$-SiPc OTFTs reported herein surpasses these results with a $m_{e,max}$ of
4.9 × 10^{-2} cm^2 V^{-1} s^{-1}, and $m_{e,avg}$ of 4.1 × 10^{-2} cm^2 V^{-1} s^{-1}, despite a notably greater V_T of 27.6 V. Axially substituted phenoxy SiPc OTFTs with a BGTC architecture fabricated by PVD have demonstrated similar electrical performance to alkyl substituted SiPcs with mobilities in the range of 10^{-3}– 10^{-2} cm^2 V^{-1} s^{-1} and threshold voltages between 20–40 V.[17] PVD fabricated $(3PS)_2$-SiPc OTFTs display similar or greater electrical performance compared to phenoxy substituted SiPcs, with the exception of F_{10}-SiPc, which to our knowledge reports the greatest $m_{e,avg}$ of 0.27 cm^2 V^{-1} s^{-1} with a V_T of 23.5 V for PVD fabricated BGTC SiPc OTFTs.[16]

Owing to the difference in crystallite nucleation and film growth between PVD and solution fabrication methods, one would expect differences in the electrical performance between OTFTs fabricated by these different processes. While crystallite growth by PVD relies on a carefully controlled deposition rate and substrate temperature, crystallite growth from solution is characterized by the rate of solvent evaporation, which is hardly controllable and typically occurs orders of magnitude faster than PVD.[26–29] The variable crystallization rate achieved by solution fabrication can lead to large crystallite formation which can negatively impact charge transport due to wider grain boundaries and a high degree of molecular disorder.[21,30] However, it is well known that charge transport is dependent not only on crystallite size but also on several other factors including grain boundary effects, surface roughness, crystallite packing, and molecular orientation, with the interplay between these parameters being crucial for achieving high mobility OTFTs.[31–34] For $(3PS)_2$-SiPc, the effects of these factors are mitigated by the efficient charge transport in the material, resulting in OTFTs with similar electrical performance irrespective of fabrication method and thin-film characteristics.

To further assess $(3PS)_2$-SiPc thin-film formation by PVD and solution fabrication, the effects of post-deposition thermal annealing were studied through OTFT electrical performance and XRD. Characteristic transfer curves of PVD (Fig. 4a) and solution (Fig. 4b) fabricated OTFTs annealed

from 25–150 °C displayed little change in m_e. However, at an annealing temperature of 150 °C a reduction in V_T was observed in all OTFTs, with PVD devices exhibiting a 7.2 V decrease from an average V_T of 26.8 V to 18.4 V, and solution devices exhibiting a greater reduction of 14.4 V from an average V_T of 34.0 V to 19.6 V. Thermogravimetric analysis (TGA) and differential scanning calorimetry (DSC) measurements of $(3PS)_2$-SiPc powder show no significant thermal events before the decomposition temperature at approximately 340 °C and no phase transitions between 25–240 °C.[24] The high thermal stability of $(3PS)_2$-SiPc, together with the three dimensional character of charge transport of polymorph 2, as revealed by DFT and KMC calculations, may be the reasons for the consistently high m_e observed in OTFTs fabricated by different methods, suggesting that thermal annealing can be used on $(3PS)_2$-SiPc devices to further improve V_T without affecting m_e.

To investigate in detail the effect of annealing on crystalline order, XRD patterns of PVD and solution fabricated $(3PS)_2$-SiPc thin-films annealed at increasing temperatures are shown in Fig. 4c and d. PVD films exhibit a primary peak at approximately 2θ= 9.00° corresponding to a *d*-spacing of 9.85 Å, and a secondary lower intensity peak at 2θ = 7.80° corresponding to a *d*-spacing of 11.35 Å. At higher annealing temperatures the intensity of the secondary peak decreases, while an increase in intensity is observed for the primary peak. In contrast, solution fabricated films exhibit a single high intensity peak at 2θ = 8.90° corresponding to a *d*-spacing of 9.96 Å when annealed at 25 °C, which shifts to 2θ = 9.02° (*d*-spacing of 9.83 Å), decreases in width, and increases in intensity when annealed at 150 1C. With both fabrication methods, thermal annealing at 150 1C results in an increase in peak intensity and shift in peak position to 2θ = 9.02°, indicating the conversion to a different crystallite packing structure. As PVD fabricated thin-films exhibit an XRD signal around 2θ = 9.00–9.02°, it is suggested that this fabrication method initially produces this packing structure; with post deposition thermal annealing the packing of additional crystallites are converted resulting in the greater peak intensity. Conversely, solution fabrication does not initially produce thin-films with this packing structure and requires thermal annealing for conversion as evidenced by the large peak shift from 2θ = 8.90° to 2θ = 9.02°.

XRD peak intensity is related to grain texture, crystallite orientation and degree of crystallinity with a higher intensity indicating a more consistently oriented thin-film.[35] Peak position is attributed to the intermolecular *d*-spacing and peak width to grain size, such that an increase in peak position along the 2θ axis represents a decrease in *d*-spacing, with a narrower peak indicating larger crystallite formation.[35] Therefore, the increase in peak intensity and shift in peak position that occurs at higher annealing temperatures indicates the formation of more highly ordered, densely packed, crystalline thin-films as evident by the reduction in intermolecular *d*-spacing and increase in peak intensity. Additionally, the narrower and higher intensity peaks exhibited by solution fabricated films suggest the films are comprised of larger crystallites compared to PVD films, which is corroborated by AFM images of PVD (Fig. 4e) and solution fabricated (Fig. 4f) $(3PS)_2$-SiPc thin-films. PVD films annealed at 25 1C show a densely packed network of small circular crystallites, with many grain boundaries and a surface roughness of 4.33 nm. In contrast, the morphology of solution fabricated films exhibits large plate like crystallites, with fewer boundaries and a surface roughness of 1.65 nm. Although there are significant differences in thin-film morpho- logy between PVD and solution fabricated $(3PS)_2$-SiPc films, both morphologies exhibit interconnected, and largely homogenous features that promote efficient charge transport.

The preicted XRD patterns (Fig. S6, ESI†) of polymorph 1 and 2 calculated from single crystal data shows two peaks at 2θ = 8.82° and 9.50° for polymorph 1 and 2θ = 8.36° and 9.14° for polymorph 2. As neither of the thin-film XRD data of PVD and solution fabricated films aligns with these peaks, we surmise that a new polymorphic form is present in films compared to powder samples. As discussed, the polymorphic nature of $(3PS)_2$-SiPc dictates the degree of charge transport with a high dimensional dependence. Both PVD and solution fabrication methods resulted in $(3PS)_2$-

SiPc thin-films with high mobilities and favourable charge transport, suggesting that the new polymorph present in films may have a similar structure to that of polymorph 2.

STXM characterization

STXM measurements at the carbon K-edge were carried out on a solution fabricated thin-film of $(3PS)_2$-SiPc with X-rays irradiated in normal incidence to the sample and measurements executed by altering the polarization of the beam between linear horizontal (LH) and linear vertical (LV) (Fig. 5a). Planar MPcs, such as SiPcs, commonly form a herringbone packing structure with alternating face-to-edge and face-to-face molecular packing oriented either or both edge-on and face-on to the substrate surface.[36–38] For the OTFT architecture used herein, edge-on orientation of the $(3PS)_2$-SiPc molecules is desired as the increased p–p stacking along this direction results in greater charge transport between the source-drain electrodes, ultimately resulting in higher mobility OTFTs.[17,21,39,40] The highly anisotropic nature and directional dependent charge transport of MPcs, in particular $(3PS)_2$-SiPc as evident by poly- morph 1 and polymorph 2 in Fig. 3, further justifies additional thin-film characterization.

Fig. 5b shows the carbon (C) 1s near edge X-ray absorption fine structure (NEXAFS) spectra of $(3PS)_2$-SiPc, which exhibits a sharp peak at 285 eV corresponding to the C 1s-p* transition of the CQC bonds, a small shoulder at approximately 288 eV corresponding to the C 1s-s* transition of the C–H bonds, and two broad contributions at 293 eV and 304 eV corresponding to the C 1s-s* transition of the C–C bonds.[41] In NEXAFS spectroscopy, the intensity of a transition is proportional to the square of the cosine of the angle between the transition vector (-p* in our case at 285 eV) and the electric field vector of the beam (E_{LV} or E_{LH} in our case).[42] Monitoring the resonance intensity as a function of the polarization can thus provide information about the local molecular orientation. The NEXAFS spectra of a $(3PS)_2$-SiPc film shows a strong dichroic behaviour with an increase in resonance from 0.28 to 0.40 of the 285 eV peak when the polarization is switched from LH to LV. This partial increase, corresponding to a C 1s-p* transition perpendicular to the SiPc plane, indicates that the molecules are not orientated purely face-on nor purely edge-on to the substrate but rather aligned in pseudo edge-on configuration. Optical density (OD) images were taken at 285 eV for both LV and LH polarizations with a LH–LV difference image generated from these (Fig. 5c and d respectively). The dichroic behaviour can be clearly seen from these images as shown by the high- lighted cluster of pixels which turns on from LH to LV, with an averaged difference in optical density of -0.1. From the LH–LV difference image, the domains of various intensity correspond to different SiPc molecular orientations, indicating the films are comprised of molecules orientated in many angles to the substrate surface. Given the small amplitude in the p* resonance intensity differences, these variations in molecular orientation are relatively small, therefore the film remains relatively homogenous throughout with $(3PS)_2$-SiPc domains on the order of 1–4 mm. This analysis demonstrates that STXM is a powerful technique that can be used to characterize MPcs thin-films and provide insight into the molecular orientation through the entire film.

Conclusion

In this work the charge transport properties of the polymorphic forms of the $(3PS)_2$-SiPc crystal were determined by KMC simulations and DFT calculations, and the differences between $(3PS)_2$-SiPc OTFTs fabricated by PVD and solution processing were accessed through electrical characterization, topographical imaging, and the determination of thin-film microstructure. OTFTs fabricated from solid state and solution methods resulted in similar performance metrics with average mobilities in the range of 1.0–3. $\times 10^{-2}$ cm^2 V^{-1} s^{-1} for PVD devices and 2.3–4.1 $\times 10^{-2}$ cm^2 V^{-1} s^{-1} for solution. Post-deposition thermal annealing was shown to have little effect on the m_e of OTFTs although a noticeable decrease in V_T at greater annealing temperature was observed across all devices, suggesting that thermal annealing can be used as a method to reduce V_T without negatively impacting m_e. Synchrotron based STXM measurements

demonstrated that the films are constituted by domains of 1–4 mm where the $(3PS)_2$-SiPc are primarily oriented in the same pseudo edge-on direction. This study demonstrates the unique ability to integrate $(3PS)_2$-SiPc into n-type OTFTs through solution and vapour fabrication techniques, providing opportunity for hybrid manufacturing.

Experimental

Materials

Bis(tri-*n*-propylsilyl oxide) silicon phthalocyanine was synthe- sized as described in literature.[24] All solvents were purchased from commercial suppliers and used as received.

Computational

Quantum chemical calculations were performed using the same levels of approximation as in our previous works.[17,20,21,30,43] Energies of the highest occupied and lowest unoccupied mole- cular orbitals (HOMO and LUMO) were obtained after optimiz- ing the molecular geometry using density functional theory (DFT) at the B3LYP/6-31G(d) level. Vertical transition energies and oscillator strengths towards the first optically allowed excited states were computed by means of time-dependent DFT with the same level of approximation. The electron affinity (EA) was obtained using the differences in the total energies of the charged and neutral molecules in their optimized geometries.

The charge transfer rates between adjacent molecules *i* and *j*

were calculated according to the semi classical rate equation due to Marcus (eqn (1)), which displays a dependence on the square of the electronic coupling J_{ij}:[44]

$$k_{ij} = \frac{2\pi}{\hbar}\frac{J_{ij}^2}{\sqrt{4\pi\lambda k_B T}}\exp\left[-\frac{(\Delta G_{ij}+\lambda)^2}{4\lambda k_B T}\right] \qquad (1)$$

where $\hbar$ and k_B are respectively the reduced Planck and Boltzmann constants, and T = 300 K. $\lambda = \lambda_i + \lambda_s$ is the reorganization energy, which includes both the fast fluctuations of the energy of the molecules and their surrounding, and $\Delta G_{ij} = -EA_j + EA_i - eE \cdot r_{ij}$ comprises the spatial (*static*) variations of electron affinities and the contribution of an external electric field E, which in turn depends on the intermolecular vector r_{ij}. The intramolecular fraction of reorganization energy (λ_i) for electron transport was obtained with the four points method[45] and B3LYP/6-31G(d) calculations. The external fraction ls was set to 0.2 eV, a value predicted for a low dielectric constant medium by continuum model calculations.[46] The electronic couplings J_{ij} were obtained by employing the projection method involving the LUMOs of monomers,[47] and assuming the degeneracy of the LUMO and LUMO+1 levels.[43] Since simulations were performed on a defect-free crystal structure, another important parameter affecting

charge mobility, the standard deviation s of the transport levels (*i.e.* the site energies EA_i and EA_j), was also empirically adjusted, with the actual EA values drawn from a Gaussian distribution. Electron mobilities were evaluated by means of Kinetic Monte Carlo (KMC) simulations based on the first reactions algorithm, performed in supercells in which the experimental X-ray crystal lattice was replicated to have roughly cubic boxes with sides of about 200 Å (polymorph 1, 6720 molecules, 20 ×12 × 14 supercell; polymorph 2, 6912 molecules, 18 × 12 × 16 supercell).

Simulated mobilities were obtained by measuring the distance travelled by a single charge in the direction of the applied electric field *E*, divided by the elapsed time *t* and the field itself:

$$\mu = \boldsymbol{r}(t)\cdot\frac{\boldsymbol{E}}{E}\frac{1}{Et} \qquad (2)$$

In practice, the distance was fixed to 5×10^6 Å, while the while the time *t* necessary to travel that distance is the actual simulation result. For each value and direction of the electric field, reported mobilities are the average of 100 KMC simulations, in which both the starting site for the charge and the site energies were randomly generated. Test calculations showing the influence of the internal reorganization energy and energetic disorder on the mobilities are reported in Fig. S1–S3 (ESI†). We also demonstrated the consistency between zero-field mobi- lities extracted from KMC simulations with s = 0 with those calculated, in previous works[17,20,21,30] using a simpler compu- tational scheme that combines Einstein's electrical mobility equation and Marcus formula for the hopping rates (Table S3, ESI†). Electronic structure calculations were performed using the ORCA[48] and Gaussian[49] programs. Transfer integrals were calculated using homemade codes.

PVD fabricated OTFTs

BGTC OTFTs with (3PS)2-SiPc deposited by PVD were fabricated on N-doped silicon substrates (15 mm 20 mm) with a 300 nm thermally grown silicon oxide dielectric layer purchased from Ossila. Substrates were first rinsed with acetone and isopropa- nol to remove the protective photoresist, followed by drying with nitrogen gas. Substrates were then cleaned by sonication in sequential baths of acetone and methanol for 5 minutes, each followed by drying with nitrogen before treatment with oxygen plasma for 15 minutes to clean and hydrolyze the surface. Plasma-treated substrates were then rinsed with water and isopropanol and dried with nitrogen before submersion in a solution of 1% v/v octyltrichlorosilane (OTS)-toluene solution. Surface treatment with OTS was carried out for 24 hours at 70 °C. OTS-treated substrates were then rinsed with toluene and isopropanol and dried under vacuum at 70 C for 1 hour. BGTC OTFTs were fabricated by first thermally depositing a 300 Å film of (3PS)2-SiPc by PVD through a square shadow mask as the active semiconducting layer at a target rate of 0.2 Å s^{-1} on room-temperature substrates using an Angstrom EvoVac thermal evaporator (P < 2 × 10^{-6} torr). Top contact source- drain electrodes were fabricated using shadow masks pur- chased from Ossila (channel length of 30 mm, channel width of 1000 mm) by depositing a 100 Å layer of manganese at a rate of 0.5 Å s^{-1} followed by depositing a 500 Å layer of silver at a rate of 1 Å s^{-1}.

Solution fabricated OTFTs

Solution processed BGTC OTFTs were fabricated on the same N-doped silicon substrates purchased from Ossila as those used for PVD fabricated OTFTs. Substrates were cleaned by sequential 5 minute long sonication baths of soapy water, distilled water, acetone and methanol, then dried with nitrogen. Substrates were then treated with air plasma for 15 minutes, before being rinsed with distilled water and isopropanol, and treated with a surface treatment of 1% v/v OTS in toluene by submersion in solution for 24 hours at 70 °C. After removal from the OTS solution, substrates were rinsed with toluene and isopropanol and dried in a vacuum oven at 70 °C for 1 hour. A 10 mg mL^{-1} $(3PS)_2$-SiPc solution in chloroform ($CHCl_3$) was prepared by heating at 50 °C for 1 hour in a nitrogen filled glovebox. The solution was then filtered through 0.2 mm pore size PTFE membrane, and deposited onto the OTS-treated substrates by spin-coating 60 mL of solution at 1500 RPM for 90 seconds. The $(3PS)_2$-SiPc films were then either thermally annealed under vacuum for 1 hour or left to dry at room temperature in nitrogen. Electrodes were deposited by PVD using an Angstrom EvoVac thermal evaporator (P < 2 × 10^{-6} torr) using the same procedure as PVD fabricated OTFTs.

OTFT characterization

Electrical characterization of OTFTs was performed as described in our previous works.[17,21] All characterization was done in a nitrogen filled glove box at room temperature using a multi tester consisting of 48 gold plated nickel probe tips that contact the source-drain and gate electrodes. A Keithley 2614B and a MCC USB DAQ was used to control the source-drain voltage (V_{SD} = 50 V) and gate voltage (0 V <V_{GS} < 60 V) to obtain source-drain current (I_{SD}) measurements in order to determine the m_e, V_T, and $I_{on/off}$.

AFM

AFM images were collected using a Bruker Dimension Icon AFM with ScanAsyst-Air tips and analyzed with NanoScope Analysis v.1.8 software.

XRD

XRD data was collected using a Rigaku Ultima IV diffractometer with Cu Ka source (λ = 1.5418 Å), a scan range of 3°< 2θ< 20° and a rate of 0.5° min^{-1} with no spin. The interplanar spacing (d-spacing) between lattice plans was calculated using Bragg's Law shown by the following equation:

$$n\lambda = 2d\,sin\theta \quad (3)$$

where λ is the wavelength of the incident wave equal to 1.54056 Å, d is the spacing between planes, θ is the angle of incidence in degrees, and n is a positive integer equal to 1 for this study.

STXM

Thin-films of $(3PS)_2$-SiPc (100 nm) were spin-coated onto a layer of poly(3,4-ethylenedioxythiophene) polystyrene sulfonate (PEDOT:PSS), floated in water and transferred onto a transmission electron microscopy (TEM) grid. STXM was performed on the HERMES beamline at the SOLEIL Synchrotron facility in Saint-Aubin, France to investigate the thin-film properties. The STXM equipment consisted of a Fresnel zone plate with 50 nm outer zone width, an order sorting aperture, the sample mounted onto a raster scanning piezo stage, and a photomultiplier tube to record the transmitted intensity. X-Rays were irradiated

in normal incidence to the sample surface and the linear polarization of the beam switched between linear horizontal (LH) and linear vertical (LV) using an undulator. Measurements were recorded in the energy range of 280–320 eV corresponding to the carbon K-edge to obtain 5 mm × 5 mm images with a step size of 50 nm and a dwell time of 3 ms. A photon energy of 285 eV with a 50 nm step size and a 3 ms dwell time was used to obtain 10 mm 10 mm images. Analysis software aXis2000 was used to process all data.[50]

Acknowledgements

Benoît H. Lessard would like to acknowledge the Natural Sciences and Engineering Research Council of Canada (NSERC, RGPIN/2015-509 03987), the University of Ottawa, and the Canada Research Chair program for financial support. C. T. thank the Ministerio de Economia y Competitividad of Spain (projects PID2019-109555GB-I00 and RED2018-102815-T) and is thankful for the technical and human support provided by DIPC Computer Center. Computer time was provided by the Mesocentre de Calcul Intensif Aquitain (MCIA) of the University of Bordeaux, financed by the Conseil Regional d'Aquitaine and the French Ministry of Research and Technology. We acknowledge the Centre for Research in Photonics at the University of Ottawa (CRPuO) for access to the AFM and Dr Jeffery Ovens for performing single crystal X-ray diffraction. The authors would like to thank the SOLEIL Synchrotron facility for providing beamtime at the HERMES beamline. SOLEIL is supported by the National Center for Scientific Research (CNRS), the French Alternative Energies and Atomic Energy Commission (CEA), the ˆIle-de-France Regional Council, the Essonne Department Council and the Centre Regional Council.

References

1 K. Kudo, M. Yamashina and T. Moriizumi, Field Effect Measurement of Organic Dye Films, *Jpn. J. Appl. Phys.*, 1984, 23(Part 1, No. 1), 130, DOI: 10.1143/JJAP.23.130.

2 F. Ebisawa, T. Kurokawa and S. Nara, Electrical Properties of Polyacetylene/Polysiloxane Interface, *J. Appl. Phys.*, 1983, 54(6), 3255–3259, DOI: 10.1063/1.332488.

3 M. E. Roberts, S. C. B. Mannsfeld, N. Queralto, C. Reese, J. Locklin, W. Knoll and Z. Bao, Water-Stable Organic Transistors and Their Application in Chemical and Biological Sensors, *Proc. Natl. Acad. Sci. U. S. A.*, 2008, 105(34), 12134–12139, DOI: 10.1073/pnas.0802105105.

4 C. Sun, X. Wang, M. A. Auwalu, S. Cheng and W. Hu, Organic Thin Film Transistors-based Biosensors, *EcoMat*, 2021, 3(2), e12094.

5 J. T. Mabeck and G. G. Malliaras, Chemical and Biological Sensors Based on Organic Thin-Film Transistors, *Anal. Bioanal. Chem.*, 2005, 384(2), 343–353, DOI: 10.1007/s00216-005-3390-2.

6 K. Baeg and J. Lee, Flexible Electronic Systems on Plastic Substrates and Textiles for Smart Wearable Technologies, *Adv. Mater. Technol.*, 2020, 5(7), 2000071, DOI: 10.1002/ admt.202000071.

7 P. Cosseddu, S. Lai and A. Bonfiglio, Highly Flexible and Low Voltage Organic Thin Film Transistors for Wearable Electronics and E-Skin Applications. In *2015 IEEE 15th International Conference on Nanotechnology (IEEE-NANO)*, IEEE, 2015, pp. 1317–1319, DOI: 10.1109/NANO.2015.7388876.

8 W. Huang, L. Feng, G. Wang and E. Reichmanis, Wearable Organic Nano-sensors. In *Flexible and Wearable Electronics for Smart Clothing*, Wiley, 2020, pp. 1–27, DOI: 10.1002/ 9783527818556.ch1.

9 L. Zhou, A. Wanga, S. C. Wu, J. Sun, S. Park and T. N. Jackson, All-Organic Active Matrix Flexible Display, *Appl. Phys. Lett.*, 2006, 88(8), 2004–2007, DOI: 10.1063/1.2178213.

10 M. Mizukami, N. Hirohata, T. Iseki, K. Ohtawara, T. Tada, S. Yagyu, T. Abe, T. Suzuki, Y. Fujisaki, Y. Inoue, S. Tokito and T. Kurita, Flexible AM OLED Panel Driven by Bottom- Contact OTFTs, *IEEE Electron Device Lett.*, 2006, 27(4), 249–251, DOI: 10.1109/LED.2006.870413.

11 Y. Fujisaki, H. Koga, Y. Nakajima, M. Nakata, H. Tsuji, T. Yamamoto, T. Kurita, M. Nogi and N. Shimidzu, Transparent Nanopaper-Based Flexible Organic Thin-Film Tran- sistor Array, *Adv. Funct. Mater.*, 2014, 24(12), 1657–1663, DOI: 10.1002/adfm.201303024.

12 Q. Meng and W. Hu, Recent Progress of N-Type Organic Semiconducting Small Molecules for Organic Field-Effect Transistors, *Phys. Chem. Chem. Phys.*, 2012, 14(41), 14152, DOI: 10.1039/c2cp41664f.

13 C. Yan, S. Barlow, Z. Wang, H. Yan, A. K.-Y. Jen, S. R. Marder and X. Zhan, Non-Fullerene Acceptors for Organic Solar Cells, *Nat. Rev. Mater.*, 2018, 3(3), 18003, DOI: 10.1038/natrevmats.2018.3.

14 C. G. Claessens, U. Hahn and T. Torres, Phthalocyanines: From Outstanding Electronic Properties to Emerging Appli- cations, *Chem. Rec.*, 2008, 8(2), 75–97, DOI: 10.1002/tcr.20139.

15 O. A. Melville, T. M. Grant, B. Mirka, N. T. Boileau, J. Park and B. H. Lessard, Ambipolarity and Air Stability of Silicon Phthalocyanine Organic Thin-Film Transistors, *Adv. Electron. Mater.*, 2019, 5(8), 1900087, DOI: 10.1002/ aelm.201900087.

16 O. A. Melville, T. M. Grant, K. Lochhead, B. King, R. Ambrose, N. A. Rice, N. T. Boileau, A. J. Peltekoff, M. Tousignant, I. G. Hill and B. H. Lessard, Contact Engineering Using Manganese, Chromium, and Bathocuproine in Group 14 Phthalocyanine Organic Thin-Film Transistors, *ACS Appl. Electron. Mater.*, 2020, 2(5), 1313–1322, DOI: 10.1021/acsaelm.0c00104.

17 B. King, O. A. Melville, N. A. Rice, S. Kashani, C. Tonnelé, H. Raboui, S. Swaraj, T. M. Grant, T. McAfee, T. P. Bender, H. Ade, F. Castet, L. Muccioli and B. H. Lessard, Silicon Phthalocyanines for N-Type Organic Thin-Film Transistors: Development of Structure–Property Relationships, *ACS Appl. Electron. Mater.*, 2021, 3(1), 325–336, DOI: 10.1021/acsaelm. 0c00871.

18 B. King, A. J. Daszczynski, N. A. Rice, A. J. Peltekoff, N. J. Yutronkie, B. H. Lessard and J. L. Brusso, Cyanophenoxy-Substituted Silicon Phthalocyanines for Low Threshold Voltage n-Type Organic Thin-Film Transistors, *ACS Appl. Electron. Mater.*, 2021, 3(5), 2212–2223, DOI: 10.1021/acsaelm.1c00175.

19 M. Faure, T. Grant and B. Lessard, Silicon Phthalocyanines as Acceptor Candidates in Mixed Solution/Evaporation Pro- cessed Planar Heterojunction Organic Photovoltaic Devices, *Coatings*, 2019, 9(3), 203, DOI: 10.3390/coatings9030203.

20 T. M. Grant, N. A. Rice, L. Muccioli, F. Castet and B. H. Lessard, Solution-Processable n-Type Tin Phthalocyanines in Organic Thin Film Transistors and as Ternary Additives in Organic Photovoltaics, *ACS Appl. Electron. Mater.*, 2019, 1(4), 494–504, DOI: 10.1021/acsaelm.8b00113.

21 R. R. Cranston, M. C. Vebber, J. F. Berbigier, N. A. Rice, C. Tonnelé, Z. J. Comeau, N. T. Boileau, J. L. Brusso, A. J. Shuhendler, F. Castet, L. Muccioli, T. L. Kelly and B. H. Lessard, Thin-Film Engineering of Solution-Processable n-Type Silicon Phthalocyanines for Organic Thin-Film Tran- sistors, *ACS Appl. Mater. Interfaces*, 2021, 13(1), 1008–1020, DOI: 10.1021/acsami.0c17657.

22 T. M. Grant, K. L. C. Kaller, T. J. Coathup, N. A. Rice, K. Hinzer and B. H. Lessard, High Voc Solution-Processed Organic Solar Cells Containing Silicon Phthalocyanine as a Non-Fullerene Electron Acceptor, *Org. Electron.*, 2020, 87, 105976, DOI: 10.1016/j.orgel.2020.105976.

23 M. C. Vebber, T. M. Grant, J. L. Brusso and B. H. Lessard, Bis(Trialkylsilyl Oxide) Silicon Phthalocyanines: Understanding the Role of Solubility in Device Performance as Ternary Additives in Organic Photovoltaics, *Langmuir*, 2020, 36(10), 2612–2621, DOI: 10.1021/acs.langmuir.9b03772.

24 T. M. Grant, C. Dindault, N. A. Rice, S. Swaraj and B. H. Lessard, Synthetically Facile Organic Solar Cells with 44% Efficiency Using P3HT and a Silicon Phthalocyanine Non-Fullerene Acceptor, *Mater. Adv.*, 2021, 2(8), 2594–2599, DOI: 10.1039/D1MA00165E.

25 B. H. Lessard, The Rise of Silicon Phthalocyanine: From Organic Photovoltaics to Organic Thin Film Transistors *ACS Appl. Mater. Interfaces*, 2021, 13(27), 31321–31330, DOI: 10.1021/acsami.1c06060

26 A. A. Virkar, S. Mannsfeld, Z. Bao and N. Stingelin, Organic Semiconductor Growth and Morphology Considerations for Organic Thin-Film Transistors, *Adv. Mater.*, 2010, 22(34), 3857–3875, DOI: 10.1002/adma.200903193.

27 V. I. Markov, *Crystal Growth for Beginners: Fundamentals of Nucleation, Crystal Growth, and Epitaxy*, World Scientific: Hackensack, New Jersey, 3rd edn, 2016.

28 Y. Diao, L. Shaw, Z. Bao and S. C. B. Mannsfeld, Morphology Control Strategies for Solution-Processed Organic Semiconductor Thin Films, *Energy Environ. Sci.*, 2014, 7(7), 2145–2159, DOI: 10.1039/c4ee00688g.

29 S. S. Lee, C. S. Kim, E. D. Gomez, B. Purushothaman, M. F. Toney, C. Wang, A. Hexemer, J. E. Anthony and Y.-L. Loo, Controlling Nucleation and Crystallization in Solution-Processed Organic Semiconductors for Thin-Film Transistors, *Adv. Mater.*, 2009, 21(35), 3605–3609, DOI: 10.1002/adma.200900705.

30 R. R. Cranston, M. C. Vebber, N. A. Rice, C. Tonnelé, F. Castet, L. Muccioli, J. L. Brusso and B. H. Lessard, N-Type Solution-Processed Tin versus Silicon Phthalocya- nines: A Comparison of Performance in Organic Thin- Film Transistors and in Organic Photovoltaics, *ACS Appl. Electron. Mater.*, 2021, 3(4), 1873–1885, DOI: 10.1021/acsaelm.1c00114.

31 J. Rivnay, S. C. B. Mannsfeld, C. E. Miller, A. Salleo and M. F. Toney, Quantitative Determination of Organic Semiconductor Microstructure from the Molecular to Device Scale, *Chem. Rev.*, 2012, 112(10), 5488–5519, DOI: 10.1021/cr3001109.

32 Y. Don Park, J. A. Lim, H. S. Lee and K. Cho, Interface Engineering in Organic Transistors, *Mater. Today*, 2007, 10(3), 46–54, DOI: 10.1016/S1369-7021(07)70019-6.

33 J. Locklin, M. E. Roberts, S. C. B. Mannsfeld and Z. Bao, Optimizing the Thin Film Morphology of Organic Field-Effect Transistors: The Influence of Molecular Structure and Vacuum Deposition Parameters on Device Performance, *J. Macromol. Sci., Polym. Rev.*, 2006, 46(1), 79–101, DOI: 10.1080/15321790500471244.

34 H. E. Katz and Z. Bao, The Physical Chemistry of Organic Field-Effect Transistors, *J. Phys. Chem. B*, 2000, 104(4), 671–678, DOI: 10.1021/jp992853n.

35 C. F. Holder and R. E. Schaak, Tutorial on Powder X-Ray Diffraction for Characterizing Nanoscale Materials, *ACS Nano*, 2019, 13(7), 7359–7365, DOI: 10.1021/acsnano. 9b05157.

36 R. R. Cranston and B. H. Lessard, Metal Phthalocyanines: Thin-Film Formation, Microstructure, and Physical Proper- ties, *RSC Adv.*, 2021, 11(35), 21716–21737, DOI: 10.1039/d1ra03853b.

37 H. Peisert, T. Schwieger, J. M. Auerhammer, M. Knupfer, M. S. Golden, J. Fink, P. R. Bressler and M. Mast, Order on Disorder: Copper Phthalocyanine Thin Films on Technical Substrates, *J. Appl. Phys.*, 2001, 90(1), 466–469, DOI: 10.1063/1.1375017.

38 I. Biswas, H. Peisert, M. B. Casu, B.-E. Schuster, P. Nagel, M. Merz, S. Schuppler and T. Chass´e, Initial Molecular Orientation of Phthalocyanines on Oxide Substrates, *Phys. Status Solidi*, 2009, 206(11), 2524–2528, DOI: 10.1002/pssa.200925111.

39 L. Li, W. Hu, H. Fuchs and L. Chi, Controlling Molecular Packing for Charge Transport in Organic Thin Films, *Adv. Energy Mater.*, 2011, 1(2), 188–193, DOI: 10.1002/ aenm.201000021.

40 L. Li, Q. Tang, H. Li and W. Hu, Molecular Orientation and Interface Compatibility for High Performance Organic Thin Film Transistor Based on Vanadyl Phthalocyanine, *J. Phys. Chem. B*, 2008, 112(34), 10405–10410, DOI: 10.1021/jp800879g.

41 C. R. McNeill and H. Ade, Soft X-Ray Characterisation of Organic Semiconductor Films, *J. Mater. Chem. C*, 2013, 1(2), 187–201, DOI: 10.1039/C2TC00001F.

42 J. Stöhr, *NEXAFS Spectroscopy; Springer Series in Surface Sciences*, Springer Berlin Heidelberg: Berlin, Heidelberg, 1992, vol. 25, DOI: 10.1007/978-3-662-02853-7.

43 S. M. Gali, M. Matta, B. H. Lessard, F. Castet and L. Muccioli, Ambipolarity and Dimensionality of Charge Transport in Crystalline Group 14 Phthalocyanines: A Com- putational Study, *J. Phys. Chem. C*, 2018, 122(5), 2554–2563, DOI: 10.1021/acs.jpcc.7b11588.

44 R. A. Marcus, Electron Transfer Reactions in Chemistry. Theory and Experiment, *Rev. Mod. Phys.*, 1993, 65(3), 599–610, DOI: 10.1103/RevModPhys.65.599.

45 V. Coropceanu, M. Malagoli, D. A. da Silva Filho, N. E. Gruhn, T. G. Bill and J. L. Br´edas, Hole- and Electron-Vibrational Couplings in Oligoacene Crystals: Intra- molecular Contributions, *Phys. Rev. Lett.*, 2002, 89(27), 1–4, DOI: 10.1103/PhysRevLett.89.275503.

46 V. Lemaur, M. Steel, D. Beljonne, J.-L. Br´edas and J. Cornil, Photoinduced Charge Generation and Recombination Dynamics in Model Donor/Acceptor Pairs for Organic Solar Cell Applications: A Full Quantum-Chemical Treatment, *J. Am. Chem. Soc.*, 2005, 127(16), 6077–6086, DOI: 10.1021/ ja042390l.

47 E. F. Valeev, V. Coropceanu, D. A. da Silva Filho, S. Salman and J.-L. Brédas, Effect of Electronic Polarization on Charge-Transport Parameters in Molecular Organic Semiconduc- tors, *J. Am. Chem. Soc.*, 2006, 128(30), 9882–9886, DOI: 10.1021/ja061827h.

48 F. Neese, The ORCA Program System, *WIREs Comput. Mol. Sci.*, 2012, 2(1), 73–78, DOI: 10.1002/wcms.81.

49 M. J. Frisch, G. W. Trucks, H. B. Schlegel, G. E. Scuseria, M. A. Robb, J. R. Cheeseman, G. Scalmani, V. Barone, G. A. Petersson, H. Nakatsuji, X. Li, M. Caricato, A. V. Marenich, J. Bloino, B. G. Janesko, R. Gomperts, B. Mennucci, H. P. Hratchian, J. V. Ortiz, A. F. Izmaylov, J. L. Sonnenberg, D. Williams-Young, F. Ding, F. Lipparini, F. Egidi, J. Goings, B. Peng, A. Petrone, T. Henderson, D. Ranasinghe, V. G. Zakrzewski, J. Gao, N. Rega, G. Zheng, W. Liang, M. Hada, M. Ehara, K. Toyota, R. Fukuda, J. Hasegawa, M. Ishida, T. Nakajima Y. Honda, O. Kitao, H. Nakai, T. Vreven, K. Throssell, J. A. Montgomery Jr., J. E. Peralta, F. Ogliaro, M. J. Bearpark, J. J. Heyd, E. N. Brothers, K. N. Kudin, V. N. Staroverov, T. A. Keith, R. Kobayashi, J. Normand, K. Raghavachari, A. P. Rendell, J. C. Burant, S. S. Iyengar, J. Tomasi, M. Cossi, J. M. Millam, M. Klene, C. Adamo, R. Cammi, J. W. Ochterski, R. L. Martin, K. Morokuma, O. Farkas, J. B. Foresman and D. J. Fox, *Gaussian 16*, Gaussian, Inc., Wallingford CT, 2016.

50 A. Hitchcock, *AXis 2000-Analysis of X-Ray Images and Spectra*, 1997.

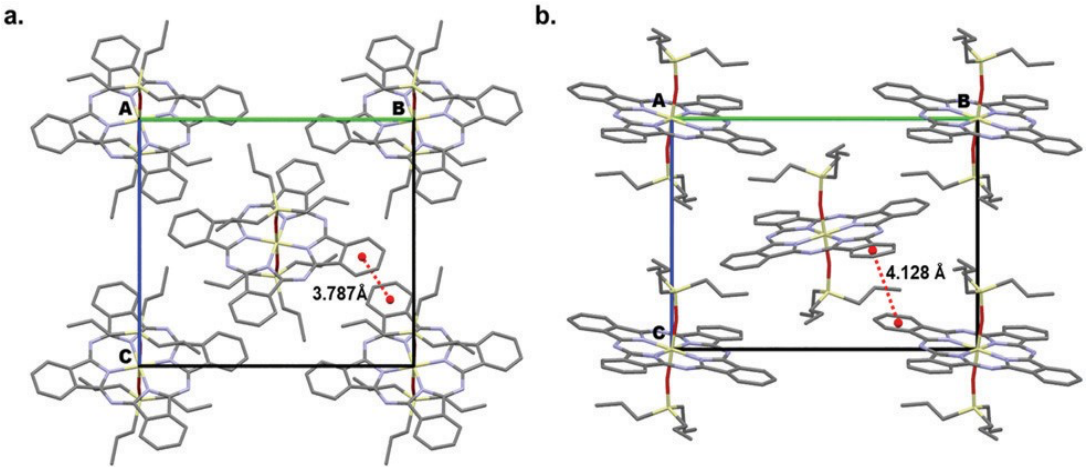

Fig. 1 Stick representation of the crystal packing of (a) polymorph 1 (CCDC# 2067659) with unit cell (A 10.23, B 16.43, c 14.62, a 90, b 108.9 c 90) and (b) polymorph 2 (CCDC# 2091746) with unit cell (A 11.26, B 17.32, c 12.52, a 90, b 101.5, c 90) of $(3PS)_2$-SiPc viewed along the *a* axis.

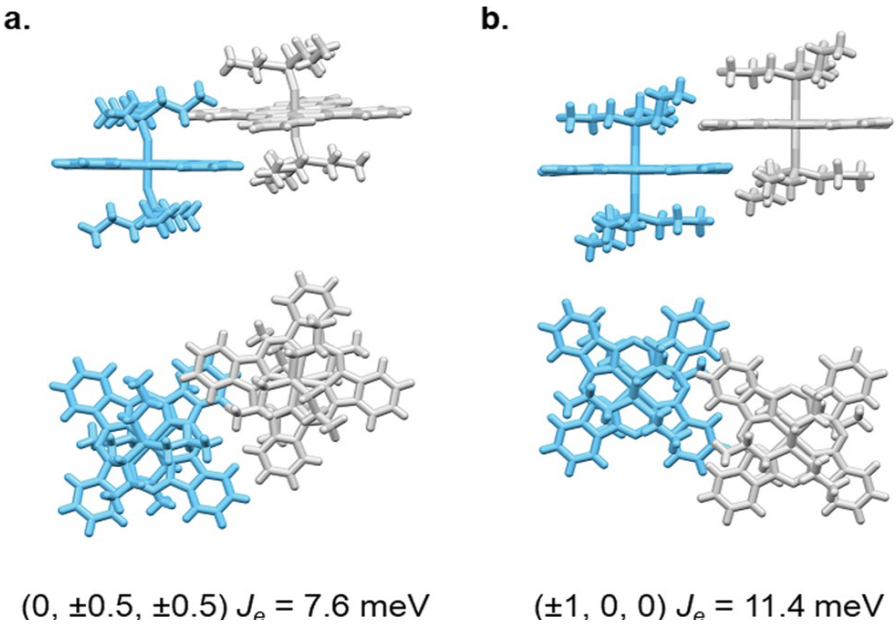

Fig. 2 Top and side views of molecular dimers giving rise to the largest electronic couplings (J_e) of (a) polymorph 1 and (b) polymorph 2 of $(3PS)_2$-SiPc.

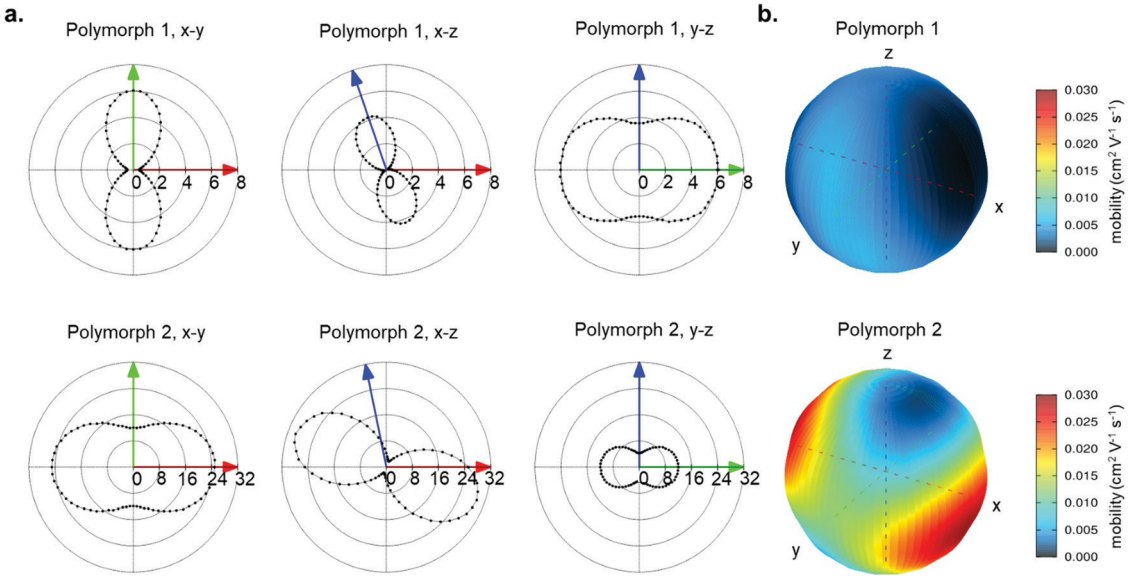

Fig. 3 (a) Polar plots of electron mobility (× 10^{-3} cm^2 V^{-1} s^{-1}) as a function of the direction of the applied electric field in the *x*–*y*, *x*–*z* and *y*–*z* planes. Red, green and blue arrows represent the projection in those planes of *a*, *b*, and *c* crystal axes, respectively. (b) 3D map of electron mobility as a function of the direction of the applied electric field. The position on the spherical surface represents the direction of the applied electric field, and the color the magnitude of mobility. Mobilities were calculated by Kinetic Monte Carlo simulations, using the Marcus model (E = 1000 V cm^{-1}, I = 0.41 eV, T = 300 K, s = 0.052 eV).

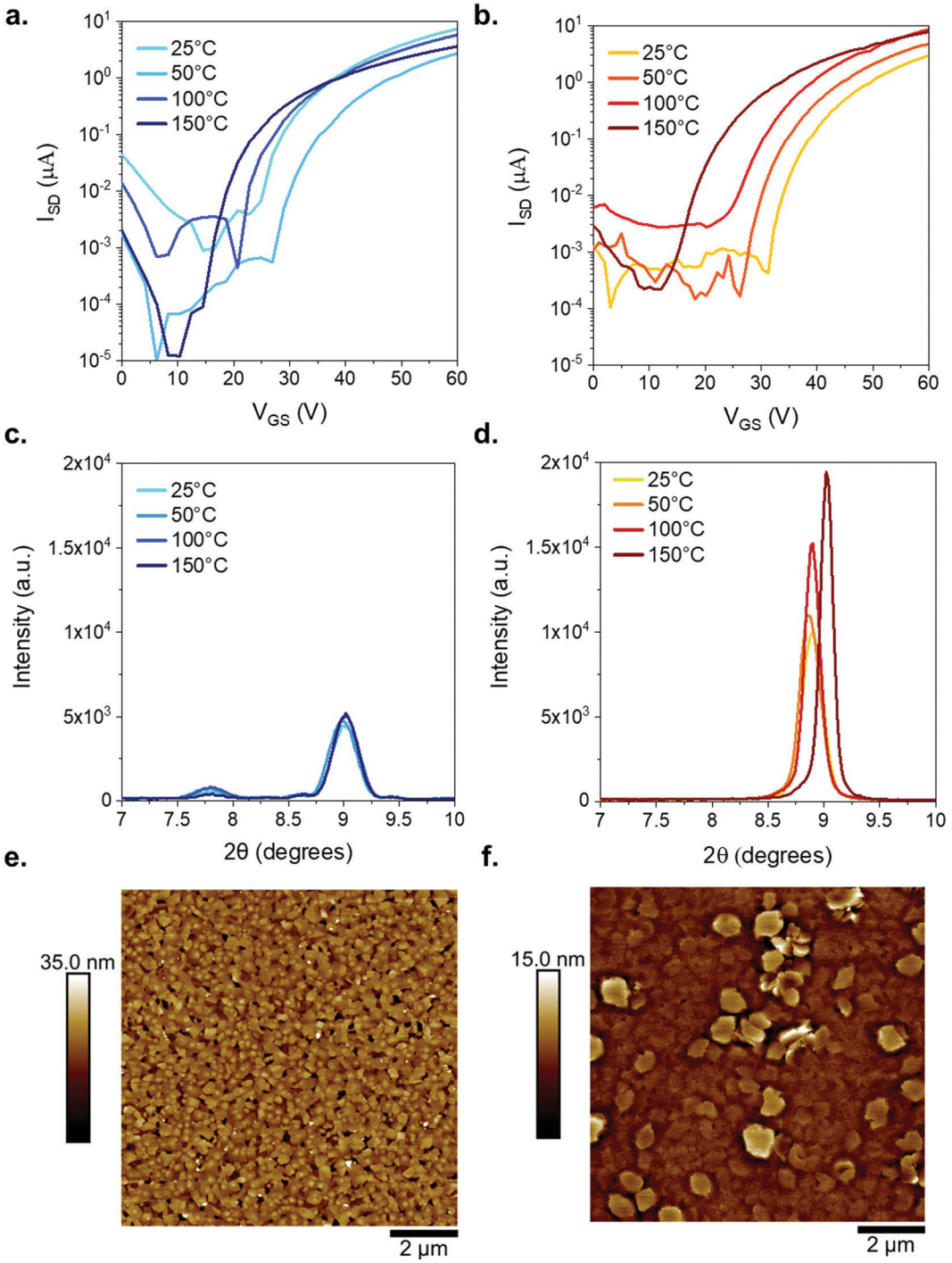

Fig. 4 Characteristic transfer curves of (a) PVD and (b) solution fabricated transistors annealed at various temperatures. XRD patterns of annealed $(3PS)_2$- SiPc thin-films fabricated by (c) PVD and (d) solution fabrication. AFM image (10 mm × 10 mm) of $(3PS)_2$-SiPc thin-films annealed at 25 °C fabricated by (e) PVD and (f) solution fabrication.

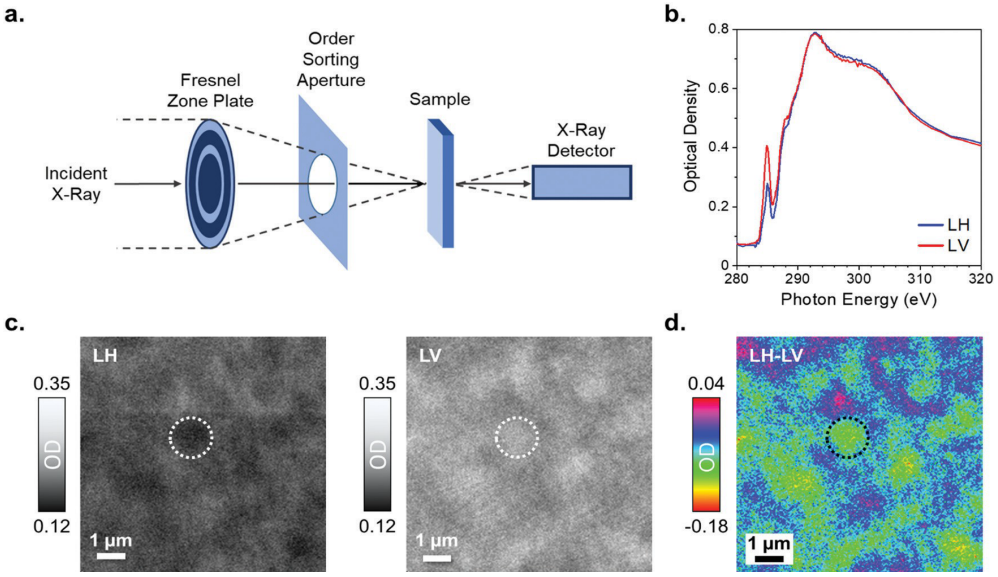

Fig. 5 (a) Schematic diagram of STXM equipment. (b) NEXAFS spectra at the carbon K-edge, (c) optical density images (10 mm × 10 mm) at 285 eV of solution fabricated $(3PS)_2$-SiPc thin-films determined by STXM and (d) LH–LV difference image generated from the optical density images.